Bulletin of the Seismological Society of America, Vol. 87, No. 4, pp. 904–917, August 1997

High-Frequency Radiation Process during Earthquake Faulting—Envelope Inversion of Acceleration Seismograms from the 1993 Hokkaido-Nansei-Oki, Japan, Earthquake

by Yasumaro Kakehi and Kojiro Irikura

Abstract We investigate the process of high-frequency (1 to 10 Hz) radiation on the fault plane of the 1993 Hokkaido-Nansei-Oki, Japan, earthquake (M_W = 7.5) from the envelope inversion of strong-motion acceleration seismograms. For the analysis, empirical Green's functions are used because theoretical approach is not available for such high frequencies. The source is modeled with two fault planes with different strike angles. The rupture process of this earthquake is very complex in terms of high-frequency wave generation. The rupture, which started on the northern fault plane, had a delay of about 10 sec or propagated very slowly between the northern and southern fault planes. High-frequency wave radiation is large at the northern and southern edges of the source region. Deceleration of rupture is also observed there. This is interpreted to be associated with stopping of rupture. Another high-frequency wave radiation area is found at the center of the northern fault plane, where discontinuity in the depth distribution of aftershocks suggests an existence of a barrier. The areas of high- and low-frequency wave radiation are not correlated. This is considered to result from the complexity of rupture process. We cannot distinguish between westward and eastward dip of the southern fault plane because of one-sided station distribution.

Introduction

The Hokkaido-Nansei-Oki, Japan, earthquake (M_W = 7.5) occurred at 13:17 GMT on 12 July 1993, very close to Okushiri Island, southwest of Hokkaido, Japan. The earthquake, subsequent tsunamis, landslides, and fires resulted in 197 deaths and 42 missing people. As this earthquake occurred at the suspected North American–Eurasian Plate boundary, knowledge of its fault plane is important for understanding the tectonics of this region. However, it became clear that the fault plane geometry was very complex and difficult to identify because different fault models were suggested by different data, such as aftershock distribution, teleseismic body waves, surface waves, geodetic data, and tsunami data.

Hino *et al.* (1994) located aftershocks using OBS data (Fig. 1). The aftershock epicentral distribution suggests that the source region is divided basically into two parts: the northern part striking SSW and the southern part striking SSE. Figure 1 also shows the topography around the Okushiri Island (Hydrographic Survey Team of Hokkaido-Nansei-Oki Earthquake, 1994) on which the aftershock epicenters are plotted. The topography has a change of strike at the same place as the aftershock distribution. However, Hino *et al.* (1994) found that the hypocentral distribution is too complicated to explain with two or three fault planes. Nakanishi *et al.* (1993) obtained different mechanisms from an analysis of *P*-wave polarities and from a moment tensor inversion of long-period (more than 70 sec) waveforms. The mechanism from *P*-wave polarities showed a westward dipping fault with a low angle (or eastward with a high angle), while their long-period wave analysis gave a mechanism dipping westward with a high angle (or eastward with a low angle), very similar to the Harvard CMT solution. This difference is because the former reflects the initial stage of rupture, but the latter describes the whole rupture process. Kuge *et al.* (1994) analyzed both teleseismic body waves and long-period surface waves. From the analysis of the body waves, using Kikuchi and Kanamori's (1991) method, they found that it was a very complicated multiple shock, whose mechanism changed during rupture propagation (Fig. 2). At the northern part of the source region, the fault plane is dipping westward with a low angle (or eastward with a high angle), while at the southern part, it is dipping westward with a high angle (or eastward with a low angle). Their long-period surface-wave analyses also support this result. They found that different mechanisms were obtained depending on whether they used for analysis both Rayleigh and Love waves or only

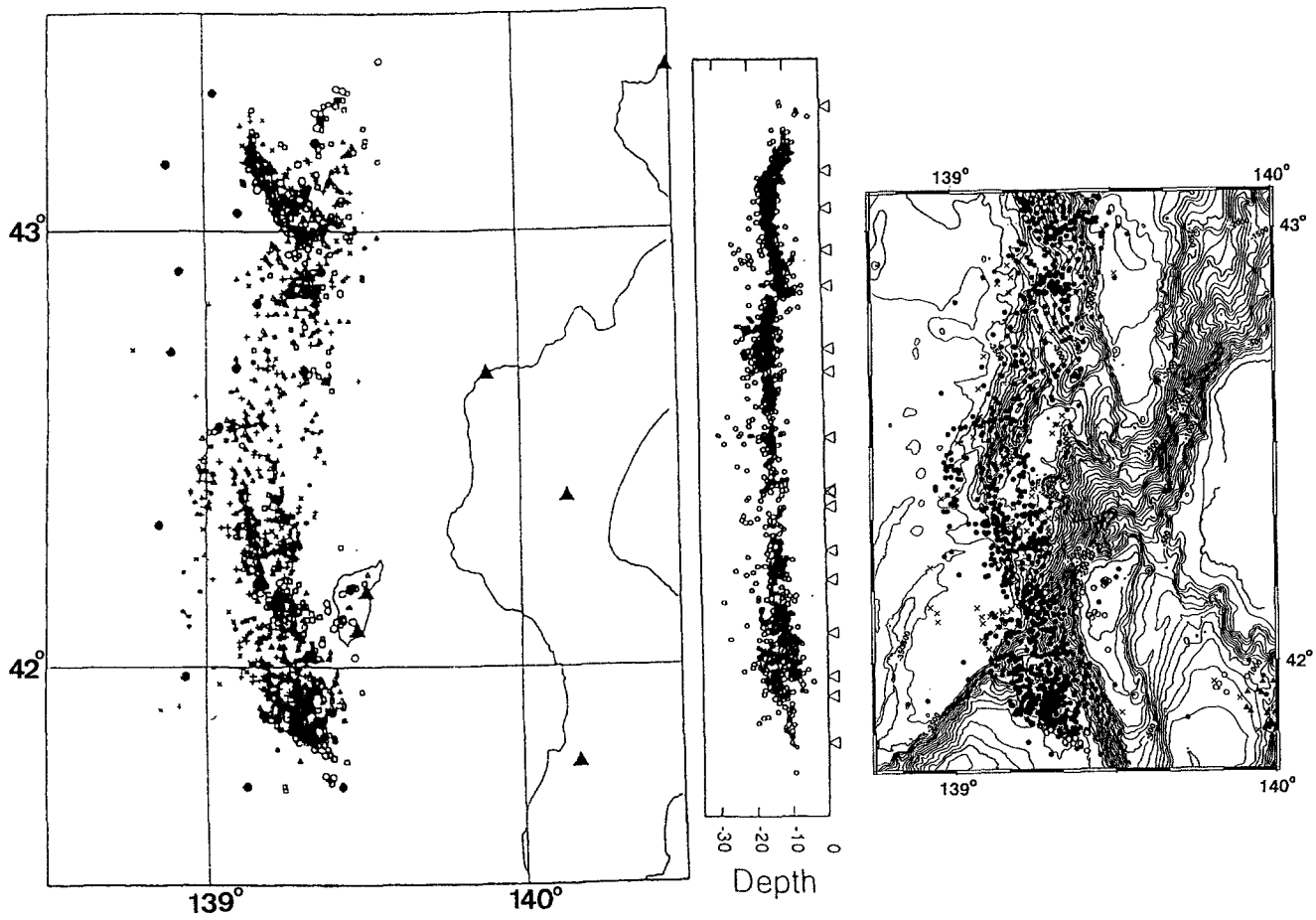

Figure 1. (Left) The aftershock hypocenters (21 July, 12:00 to 16 August, 23:59) located from the OBS observation (Hino *et al.*, 1994). Solid circles are OBS stations. (Right) The topography around Okushiri Island (Hydrographic Survey Team of Hokkaido-Nansei-Oki Earthquake, 1994) with the aftershock epicenters by Hino *et al.* (1994).

Rayleigh waves. They showed, from simple numerical simulations, that the difference was due to the mechanism change during the source process. Umino and Hasegawa (1994) determined aftershock locations using the *sP* phase and showed that their depth distribution dipped westward in the southern region. Hashimoto *et al.* (1994) presented a model composed of three fault planes (two for the southern part), all of which are dipping westward, to explain geodetic data on Okushiri Island. Their northernmost and central planes have low dip angles (20° and 30°) and the southernmost plane has a high dip angle (55°). From analysis of tsunami data, Imamura *et al.* (1994) presented a model composed of two fault planes. Though they could not determine the direction of dipping of the northern fault plane, they reported that the southern fault plane must dip eastward in order to explain the tidal record at Esashi, close to the southern source region.

The complexity of the rupture process is also easily seen in the strong ground motion acceleration seismograms observed within 200 km from the source region (Fig. 3). Since near-field data have better spatial resolution than teleseismic data, analysis of these accelerograms is very appropriate for estimating the complex rupture process of the Hokkaido-Nansei-Oki earthquake. Moreover, the determination of high-frequency wave radiation areas on the fault plane will contribute greatly to the understanding of the dynamics of rupture, because high-frequency wave radiation is related to the irregularity of rupture propagation.

Major developments in the 1980s in the source inversion techniques allowed derivation of detailed source processes from the analyses of seismic waveforms (e.g., Kikuchi and Fukao, 1985). In particular, the usage of near-field data made it possible to determine the rupture processes of earthquakes with high accuracy and resolution (e.g., Hartzell and Heaton, 1983; Fukuyama and Irikura, 1986; Mendoza and Hartzell, 1989). However, the high-frequency coverage of source process studies by the analysis of seismic waveforms has been limited to about 1 Hz. To obtain further understanding of the earthquake dynamic rupture process, analysis using higher-frequency waves is required. Also, for

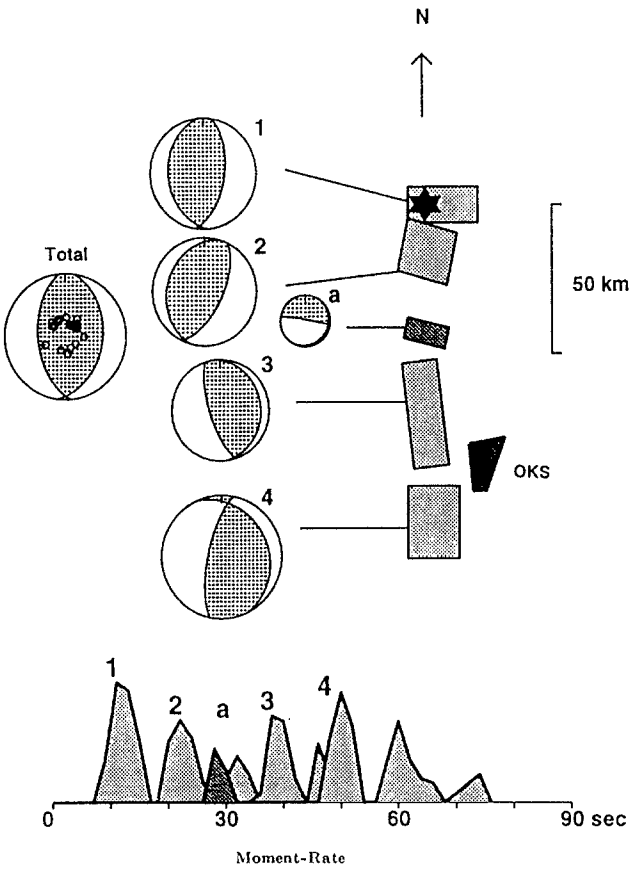

Figure 2. The spatial and temporal distribution of subevents obtained from the teleseismic body-wave inversion (Kuge *et al.*, 1994).

earthquake engineering, we need to know from what part of the fault plane seismic waves higher than 1 Hz are radiated, because those frequencies have a strong effect on common low-rise structures. Kakehi and Irikura (1996) developed a new method to determine high-frequency wave radiation areas on the fault plane from the envelope inversion of acceleration seismograms. In this method, we adopted the empirical approach for calculating the Green's function because it was impossible to obtain sufficient accuracy theoretically. Envelopes are used as inversion data instead of waveforms that are too oscillatory to be inverted. We applied this method to the 1993 Kushiro-Oki, Japan, earthquake (M_W = 7.3) and obtained the interesting result that high-frequency (2 to 10 Hz) waves were radiated mainly from near the periphery of the fault plane, while the slip distribution (Takeo *et al.*, 1993), related to lower-frequency radiation, was concentrated in the center of the fault plane.

Here we apply this method to the 1993 Hokkaido-Nansei-Oki earthquake to estimate high-frequency wave radiation areas on the fault plane. We discuss the dynamics of the rupture in terms of the results.

Method

A detailed explanation of the envelope inversion method is in Kakehi and Irikura (1996). Here we give only a brief explanation. We use the envelopes of acceleration seismograms as source inversion data. The envelopes are calculated as the running root mean square of acceleration seismograms with a given time window length. This smoothing procedure allows an inversion for frequency greater than 1 Hz, but it reduces the inversion resolution. The model parameters are the weights and rupture times of the meshes into which the fault plane is divided.

The synthetic waveform of the target event is calculated from superposition of the small-event seismogram used as an empirical Green's function, following Irikura (1986). In order to satisfy the scaling law, N^3 small-event seismograms are superposed, where N is the common ratio of fault length, fault width, and slip between the target and small events. From the scaling law, the following relation is obtained:

$$\overline{U}_L/\overline{U}_S = M_{0_L}/M_{0_S} = cN^3. \quad (1)$$

Here, $\overline{U}$ is the flat level of the displacement spectrum at low frequencies and M_0 is the seismic moment. c is the stress drop ratio between large and small events:

$$c = \Delta\sigma_L/\Delta\sigma_S. \quad (2)$$

Subscripts L and S indicate large and small events. Further,

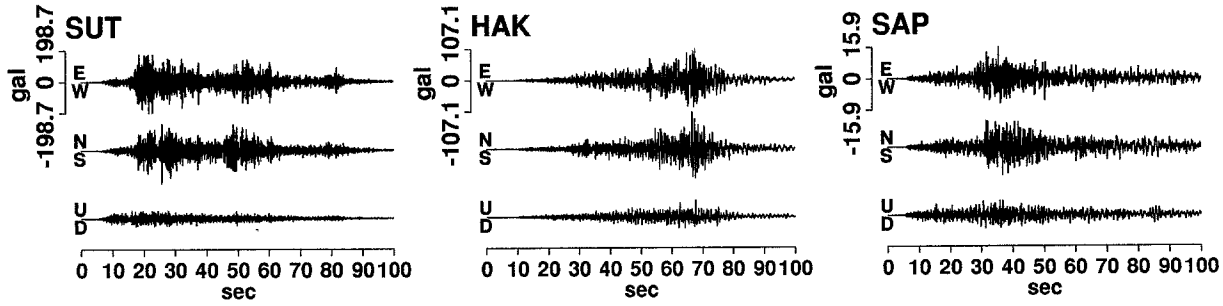

Figure 3. The observed acceleration waveforms of the 1993 Hokkaido-Nansei-Oki earthquake. They are bandpass filtered between 1 and 10 Hz.

Table 1
Parameters of the Aftershocks Used as Empirically Green's Function

Event No.	Origin Time (GMT)	Lat. (deg)	Long. (deg)	M_{JMA}	M_0(*10^{17}N-m)	f_c (Hz)	L (km)*	Area	Station
1	12 July 1994 14:45	43.10	139.23	6.0	4.2	0.33	7.6	northern area	HAK, SAP
2	12 July 1994 16:01	42.72	139.33	6.1	8.9	0.33	7.6	central area	SUT, HAK, SAP
3	14 July 1994 17:38	43.17	139.01	5.2	0.63	0.83	3.0	northern area	SUT
4	7 Aug. 1994 19:42	41.96	139.89	6.3	20	0.33	7.6	southern area	SUT, HAK, SAP

*L is a rough estimation of source size calculated by $L = (\pi r^2)^{1/2}$, where r is obtained from Brune's (1970, 1971) formula: $r = 0.373\beta/f$.

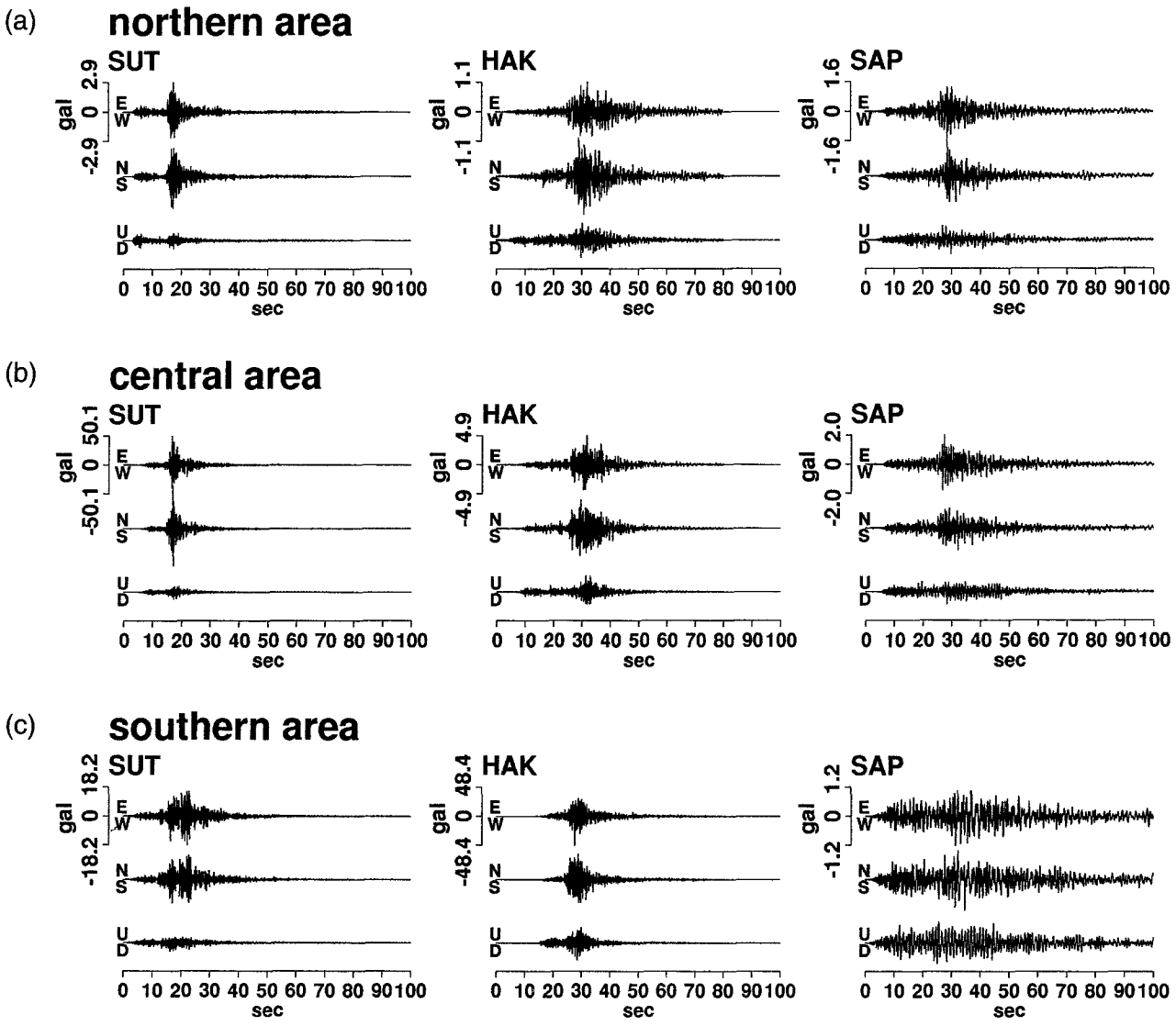

Figure 4. The aftershock acceleration waveforms used as empirical Green's functions. They are bandpass filtered between 1 and 10 Hz. Events 3 (for SUT) and 1 (for HAK and SAP) are used for the (a) northern area, event 2 is used for the (b) central area, and event 4 is used for the (c) southern area.

if their spectra follow the ω^{-2} model, the following relation is obtained:

$$\bar{A}_L/\bar{A}_S = cN. \quad (3)$$

Here $\bar{A}$ is the flat level of the acceleration spectrum at high frequencies. From (1) and (3), we can obtain N and c.

Since the ratios in fault length, fault width, and slip between the large and small events are not exactly the same, we use $NX \times NW \times NT$ instead of N^3. The fault plane of the large event is divided into $NX \times NW$ subfaults, with NX divisions along the strike direction and NW along the dip direction. The size of the subfault corresponds to that of the small-event fault plane. In each subfault NT small-event seismograms are summed using the transfer function

$$F_{ij}(t) = \delta(t - t_{ij}) + 1/n' \sum_{k=1}^{(NT-1)n'} \delta[t - t_{ij} - \{(k-1)\tau_L\}/\{(NT-1)n'\}], \quad (4)$$

$$t_{ij} = (r_{ij} - r_0)/\beta + s_{ij}. \quad (5)$$

The synthetic waveform is obtained from superposition:

$$A(t) = c \cdot \sum_{i=1}^{NX} \sum_{j=1}^{NW} w_{ij} \cdot (r/r_{ij}) \cdot F_{ij}(t) * a(t). \quad (6)$$

Here, τ_L is the rise time of the large event and β is the S-wave velocity. r_0, r, and r_{ij} are the hypocentral distances of the small event, the large event, and the subfault (i,j), respectively. n' is a parameter chosen to be much larger than NT in order to remove the artificial period that appears in relation to $\tau_L/(NT-1)$. The asterisk denotes convolution. w_{ij} and s_{ij} are the weight and rupture time of subfault (i,j), respectively. These are the model parameters to be obtained from the envelope inversion. A non-negative constraint is given to w_{ij} using the algorithm of Lawson and Hanson (1974), because sign is meaningless due to the procedure to take running root mean squares.

This inversion is nonlinear because the time variable s_{ij} is included in the model parameters and the calculation of root mean squares is nonlinear. Therefore, the inversion is linearized and solved iteratively. First, synthetic acceleration waveforms are calculated by the empirical Green's function method based on the model obtained in the previous stage of iteration. Next, envelopes of the synthetic waveforms are calculated. Then w_{ij} and s_{ij} are determined to minimize the difference between observed and synthetic envelopes in the least-squares sense with a non-negative constraint for w_{ij}. The obtained w_{ij} and s_{ij} are regarded as the final solution on convergence; otherwise, they are used as the initial model for the next iteration stage. As we are analyzing high-frequency accelerations, w_{ij} represents the weight of contribution of each mesh to the high-frequency acceleration envelope amplitude. Therefore, w_{ij} is called the acceleration radiation intensity. Heterogeneity of the high-frequency wave radiation is expressed by the distribution of w_{ij}.

We correct for attenuation on synthetic accelerations. Hoshiba (1993) obtained Q_s^{-1}, Q_i^{-1}, and $Q_t^{-1} = Q_s^{-1} + Q_i^{-1}$ from his multiple-lapse time window analysis of earthquakes in Japan whose hypocentral distances and focal depths are less than 120 and 40 km, respectively. His result shows that Q_t has a linear dependence on frequency for >1 Hz. We use $Q_t = 100f$ from his result for the Aomori station, which is closest to the source region of the Hokkaido-Nansei-Oki earthquake. The inversion is insensitive to the value of Q_t, as is verified by trying the case of $Q_t = 200f$ also. Correction of the Q effect is performed as follows. First, the acceleration data are Fourier transformed by FFT. In the frequency domain, the Fourier amplitude is corrected considering the attenuation by Q effect. Then the corrected time domain data are obtained by inverse Fourier transformation.

Data and Analysis

We use the acceleration records from the JMA (Japan Meteorological Agency) stations: Suttsu (SUT), Hakodate (HAK), and Sapporo (SAP). Four aftershocks are adopted as empirical Green's function events. As shown in Table 1, three empirical Green's functions, each of which covers the northern part, central part, and southern part of the source area, are used for producing synthetic waveforms at each station. The acceleration records are bandpass filtered between 1 and 10 Hz for the analysis. Figure 4 shows the aftershock records used as empirical Green's function. Since HAK did not record the mainshock, we use the acceleration record from the station of BRI in Hakodate (Building Research Institute), which is 2.3 km from HAK of JMA, for the mainshock. Figure 5 shows the spectral ratio between the

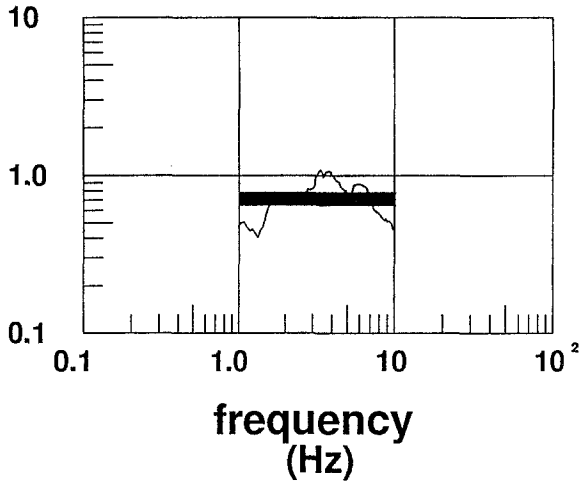

Figure 5. The spectral ratio between the records of event 4 observed at the Hakodate station of JMA and at the one of BRI. Spectrum is calculated from vectoral summation of spectra for the three components. Solid line marks a level of 0.7.

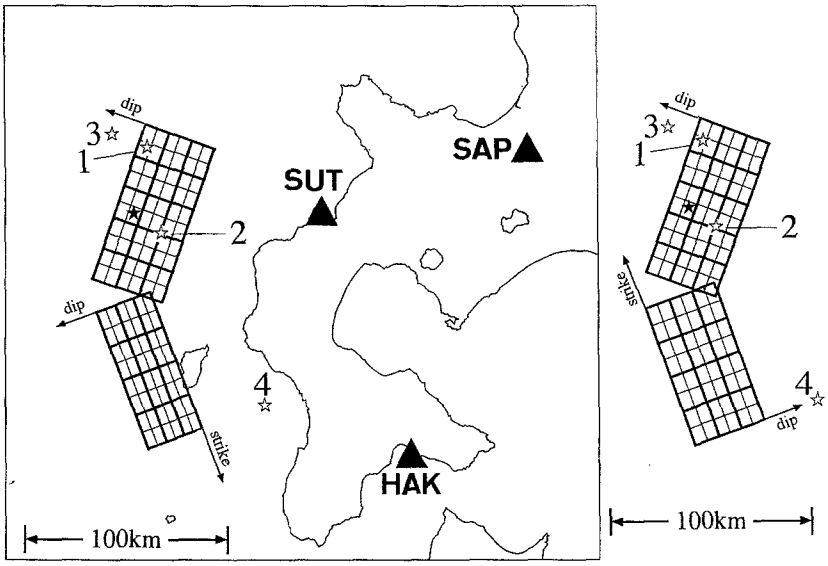

Figure 6. The station locations (triangles) and the two different fault plane models used in this study. The model on the left has the southern fault dipping westward with 30° dip angle; the model on the right has the southern fault dipping eastward with 55° dip angle. Solid star shows the rupture starting point. Open stars are the epicenters of the empirical Green's function events.

record of the number 4 event from the station of JMA and the one from the station of BRI at Hakodate. The spectral level between 1 and 10 Hz at the station of JMA is 0.7 times as large as that of the station of BRI. This is considered to express difference of amplifications between them. We use the mainshock record from the Hakodate station of BRI with a correction factor of 0.7.

Results from all kinds of data, such as aftershock distribution, mechanisms obtained from waveform inversion, tsunamis, and geodetic data, agree in that the source is very complex. Moreover, different kinds of data suggest different fault plane models, particularly for the southern half of the source area. However, we want to use as simple a model as possible for source inversion. We use a simple model based mainly on the aftershock distribution (Hino *et al.*, 1994) and the result from multiple-shock analysis using body waves (Kuge *et al.*, 1994) and abandon attempts for a model satisfying all the data. We adopt a model composed of two fault planes because the source area is roughly divided into two parts: the northern part striking SSW and the southern part striking SSE, according to the epicentral distribution of aftershocks. For the northern part, all the data suggest a fault plane dipping westward with a low angle. We determine a strike angle of 200° from the aftershock distribution, consistent with those of the first and second subevents of Kuge *et al.* (1994). Based on the dip angles (34° and 28°) of the first and second subevents of Kuge *et al.* (1994), we adopt a dip angle of 30°.

For the southern part, we cannot find a conclusive evidence to determine whether it is dipping westward or eastward. Hashimoto *et al.* (1994) presented a model composed of three fault planes (two for the southern part), all of which are dipping westward, to explain the geodetic data on Okushiri Island. On the other hand, the model presented by Imamura *et al.* (1994), from the analysis of tsunami data, has a southern fault dipping eastward. Therefore, we try two different models for the southern fault; one dipping westward and the other eastward. Dip angles of 55° (strike angle of 160°) and 30° (strike angle of 340°) are adopted, because Kuge *et al.*'s (1994) result suggests a large westward dip angle and small eastward one. Though their westward dip

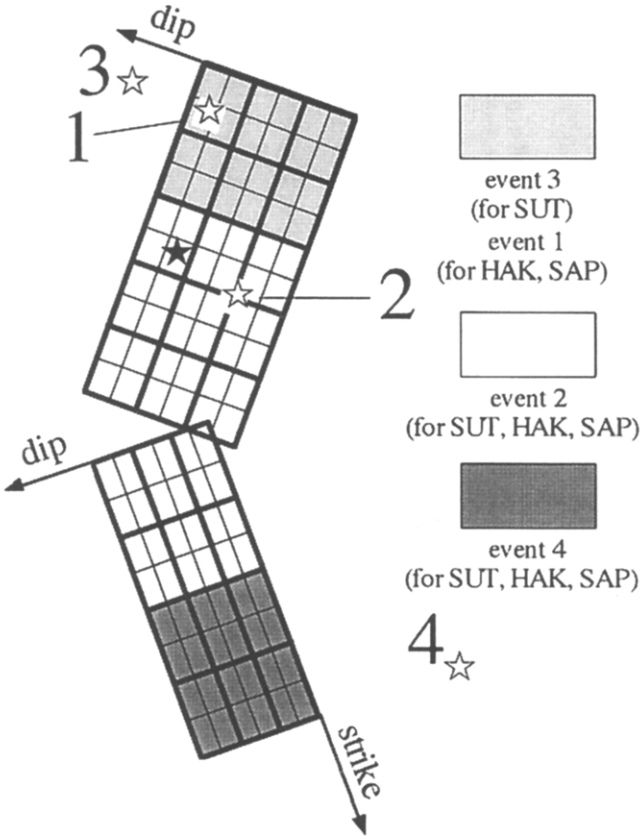

Figure 7. The three areas of the fault plane (marked with different tones), in each of which different empirical Green's function event is assigned.

angles for the third and fourth subevents are 73° and 72°, we use a smaller value of 55° consistent with the depth extent of the aftershock distribution of Hino *et al.* (1994). The fault plane sizes are determined based on the epicentral distribution and depth extent of aftershocks as follows: 80 × 42 km for the northern plane, 72 × 48 km for the southern plane dipping westward, and 72 × 42 km for the one dipping eastward. Our fault model is shown in Figure 6. The depth of the rupture starting point, denoted by a solid star, is 23 km. Our two-fault-plane models are intentionally simple and are not necessarily consistent with Hino *et al.*'s (1994) interpretation of aftershock distribution or Kuge *et al.*'s (1994) result. As mentioned later, we cannot determine which model is better. This may be because the stations are located on the same side of the source region, and sufficient resolution is not obtained for the direction of fault width.

Table 1 lists the aftershocks used for the analysis, their seismic moments, and rupture durations. These seismic moments and durations are obtained from the comparison between the observed and synthetic displacements. The table also lists a rough estimation of the source sizes, as calculated from the corner frequencies (reciprocals of durations) using Brune's (1970, 1971) formula. As explained in the previous section, when the target event is a single shock, the parameters N and c used for making synthetic waveforms from small-event records are determined from the moment ratio and high-frequency spectral ratio. The Hokkaido-Nansei-Oki earthquake is a very complex multiple shock, and although we need to separate it into subevents and calculate N and c for each of them, that is not possible because the seismic waves from different subevents are not separated but superposed on the near-field seismograms. Therefore, we take a different approach. First, $NX \times NW$, numbers of division into subfaults, are determined 10×6 for the northern fault plane and 8×6 for the southern one based on the rough estimation of the aftershock source sizes in Table 1. In Figure 7, the three areas covered by the different empirical Green's function events are shown. The northernmost area is covered by event 3 for SUT and by event 1 for HAK and SAP. As event 3 is about half the size of event 1, in order to use the same subfault size, we prepare synthetic waveforms by summing up $2 \times 2 \times 2$ records of event 3 based on the same procedure and use them as the Green's function. Next, NT and c are determined as follows. As mentioned above, it is impossible to take moment and high-frequency spectral ratios for each subevent; it is possible only for the first sub-

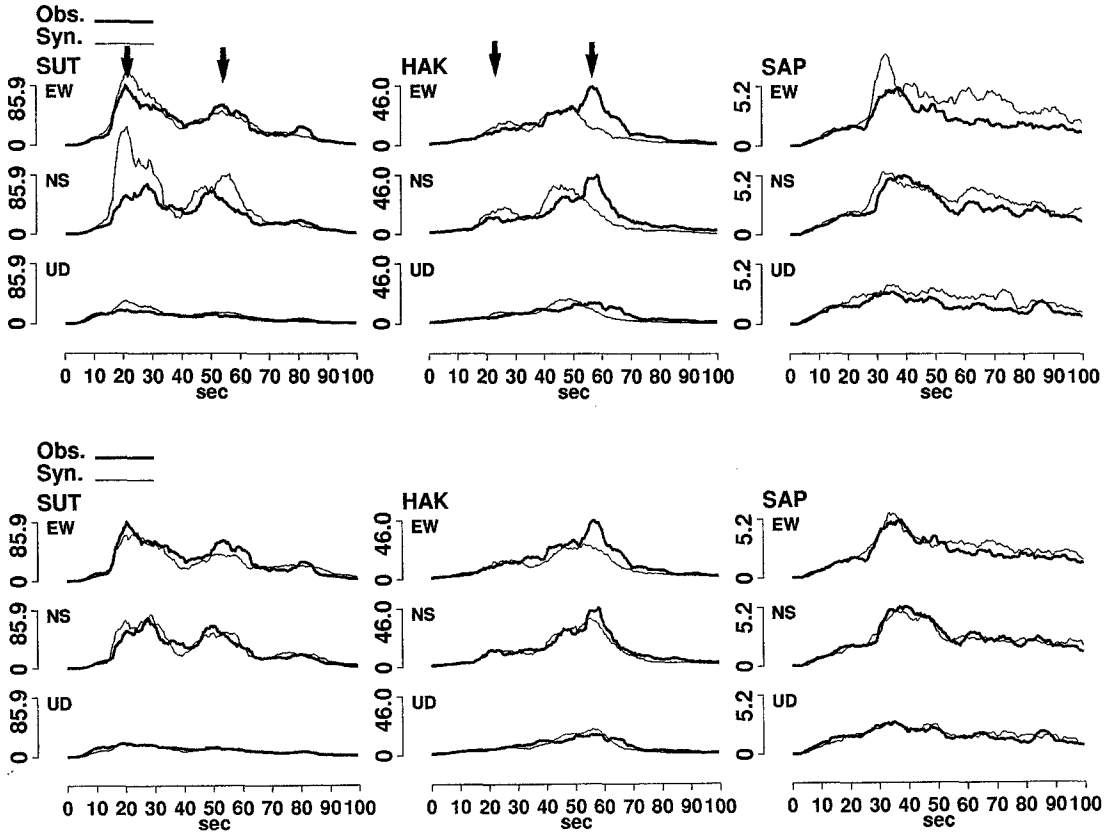

Figure 8. (Upper) Comparison of the observed envelopes and the synthetic ones for the initial model for the westward-dipping southern fault. (Lower) Comparison of the observed envelopes and the synthetic ones for the final solution. The rms window length used for the calculation of envelopes is 5 sec. Two peaks corresponding to the waves from the northern and southern fault planes are indicated with arrows.

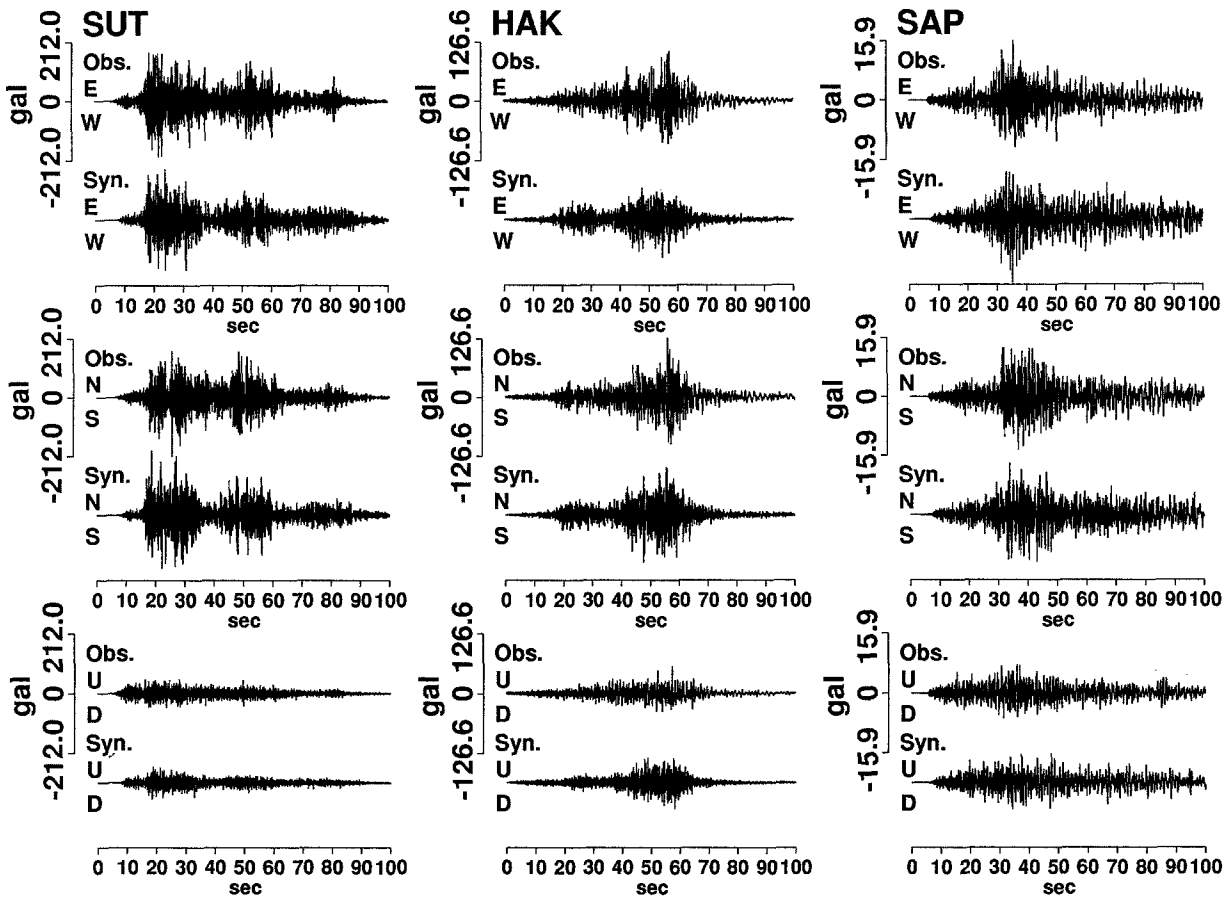

Figure 9. Comparison of the observed acceleration waveforms and the synthetic ones for the final solution for the westward-dipping southern fault.

event because seismic waves from it are little contaminated by those from subsequent subevents even in the near-field seismograms. We calculate the moment ratio between the first subevent of Kuge *et al.* (1994) and our event 2 for the area around the rupture starting point and obtained a value of 110. The spectral ratio is calculated for the first 20 sec of S waves of the mainshock and event 2 at each station. The spectrum of each event is calculated from vectoral summation of spectra for the three components. The average ratio at 1 to 10 Hz is 9.1. From (1) and (3), $N \sim 3.5$ and $c \sim 2.6$ are obtained. In the actual simulation, after several trials, we use $NT = 4$ and $c = 2.3$ for the part covered by event 2. After fixing c for event 2, we determine c for other events as follows. For event 1, we select a subfault at the boundary between the northern and central areas. Then we calculate the contributions of that subfault to the records of SAP and HAK for two cases: one with event 1 as the empirical Green's function and the other with event 2. The value of c for event 1 is determined so that the amplitudes at SAP and SUT are the same for both cases. In this way, we obtain $c = 0.71$, 0.23, and 1.2 for events 1, 3, and 4, respectively. We use $NT = 4$ for events 1 and 4, and for the Green's functions made from event 3. Other parameters used for the analysis are $\tau_L = 3.2$ sec, $\beta = 3.7$ km/sec, and $n' = 60$.

Fukuyama (1994) estimated the source-time function of event 4 by deconvolution using smaller-event records. Their result is that event 4 is a multiple shock composed of two small and one large subevents. Iwata *et al.* (1994), however, from the waveform inversion of near-field displacements, reported that it is composed of two subevents, one is much smaller than the other. They also simulated the near-field acceleration waveforms by forward modeling using the empirical Green's function method and found that the accelerations were well explained by the main event only. Therefore, it is acceptable to take event 4 as a single shock, as far as high-frequency accelerations are concerned.

In order to reduce the number of model parameters, we treat four subfaults (subfault size corresponds to that of the empirical Green's function event) as one mesh for envelope inversion as shown in Figure 7. The initial model of acceleration radiation intensities is the uniform distribution over the fault plane. The initial values of rupture times are for radial rupture propagation with a constant rupture velocity of 2.8 km/sec. The rms window length used for the calcu-

lation of envelopes is 5 sec. As the inversion is nonlinear as mentioned above, it is solved iteratively.

Results and Discussion

As discussed above, we try two kinds of fault plane models. First, we show the envelopes for the case of the southern fault dipping westward. In the upper panel of Figure 8, the observed envelopes and the synthetic envelopes for the initial model are compared. Here, it should be noted that the observed envelopes at SUT and HAK have two peaks indicated with arrows, with the second one much larger than the first at HAK. If we assume continuous rupture propagation between the northern and southern fault planes, we cannot explain the arrival time of the second peak. Therefore, we put a delay of rupture between the northern and southern fault planes in the initial model. We tried inversions with delays of 6, 8, 10, 12, and 14 sec and chose the delay of 10 sec, which brought the minimum residual. In the lower panel of Figure 8, the synthetic envelopes for the final solution are shown with the observed. The shapes of the envelopes at the first peak at SUT are improved. The amplitudes of the second peak at HAK increased to fit the observed. At SAP, the duration of the main bump, which is made of superposition of waves from the northern and southern fault planes, increased to fit the observed. The residual is reduced to 20% of the one for the initial model. Here, residual is defined as

$$\text{Res.} = \sum_{ist=1}^{3} \int \{O_{ist}(t) - S_{ist}(t)\}^2 / M_{ist}^2 dt, \qquad (7)$$

where $O_{ist}(t)$ and $S_{ist}(t)$ are the observed and synthetic envelopes at the *ist*-th station, respectively. M_{ist} is the maximum amplitude of the $O_{ist}(t)$. In Figure 9, the synthetic acceleration waveforms for the final solution are compared with the observed. The features of the observed waveforms are reproduced very well. Figure 10 shows the comparison of the observed and synthetic envelopes for the final solution for the case of the southern fault dipping eastward. Its residual is 21%, where we take that for the initial model of the other fault model as 100%. Since the residuals of the two models are very similar, we cannot conclude which model is to be preferred. This may be because the stations are located on the same side of the source region, and the dataset does not have enough resolution for the direction of the fault width. Figure 11 shows the final solutions for the two models. The acceleration radiation intensities are shown with tones, where darker tones indicate larger intensities. The distribution of acceleration radiation intensity is heterogeneous. This means that, as was expected from the observed seismograms, the rupture process of this earthquake was complex in terms of high-frequency wave radiation. Large intensities are seen at the northern and southern edge of the source region. We can interpret the high-frequency wave radiation in these areas as associated with stopping of the rupture caused by barriers. Moreover, the rupture times in these areas are 1 to 4 sec larger than the initial values; that is, the rupture propagation decelerated. This also suggests that the rupture stopped due to barriers.

Another area at the center of the northern fault or a little to the north of the center also has a large high-frequency radiation. Since it is not located at the edge of the source region, we cannot relate it to a stopping of the rupture. But this area is coincident with a clear discontinuity in depth distribution of aftershocks (Hino *et al.*, 1994) (Fig. 12). The existence of this discontinuity, which suggests a strong heterogeneity in the medium, is reliable because they determined the aftershock hypocenters from the records of OBS covering the source region. We propose that this heterogeneity is the cause of the high-frequency radiation. In this area in the northern half part of the northern fault plane, there is not only large radiation of high-frequency waves but also high aftershock activity. The may be associated, but the relation is not simple because there is an area with small high-frequency radiation and high aftershock activity on the southern fault plane.

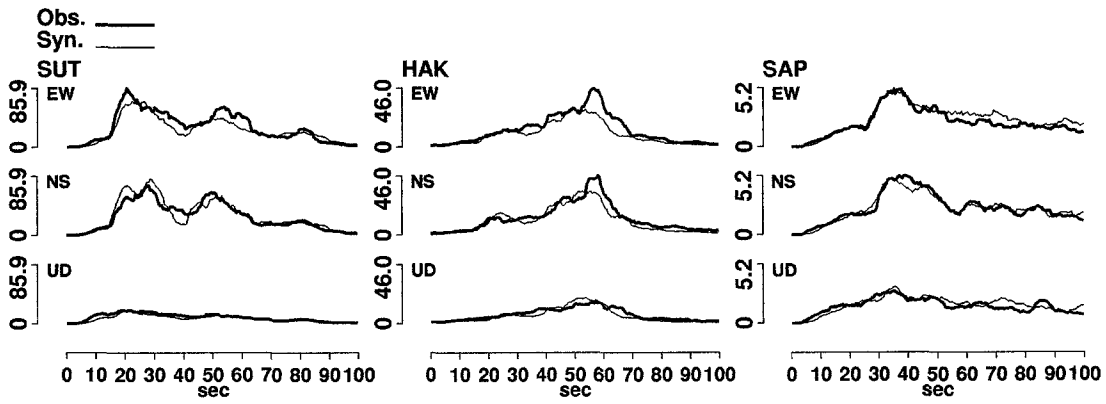

Figure 10. Comparison of the observed envelopes and the synthetic ones for the final solution for the eastward-dipping southern fault.

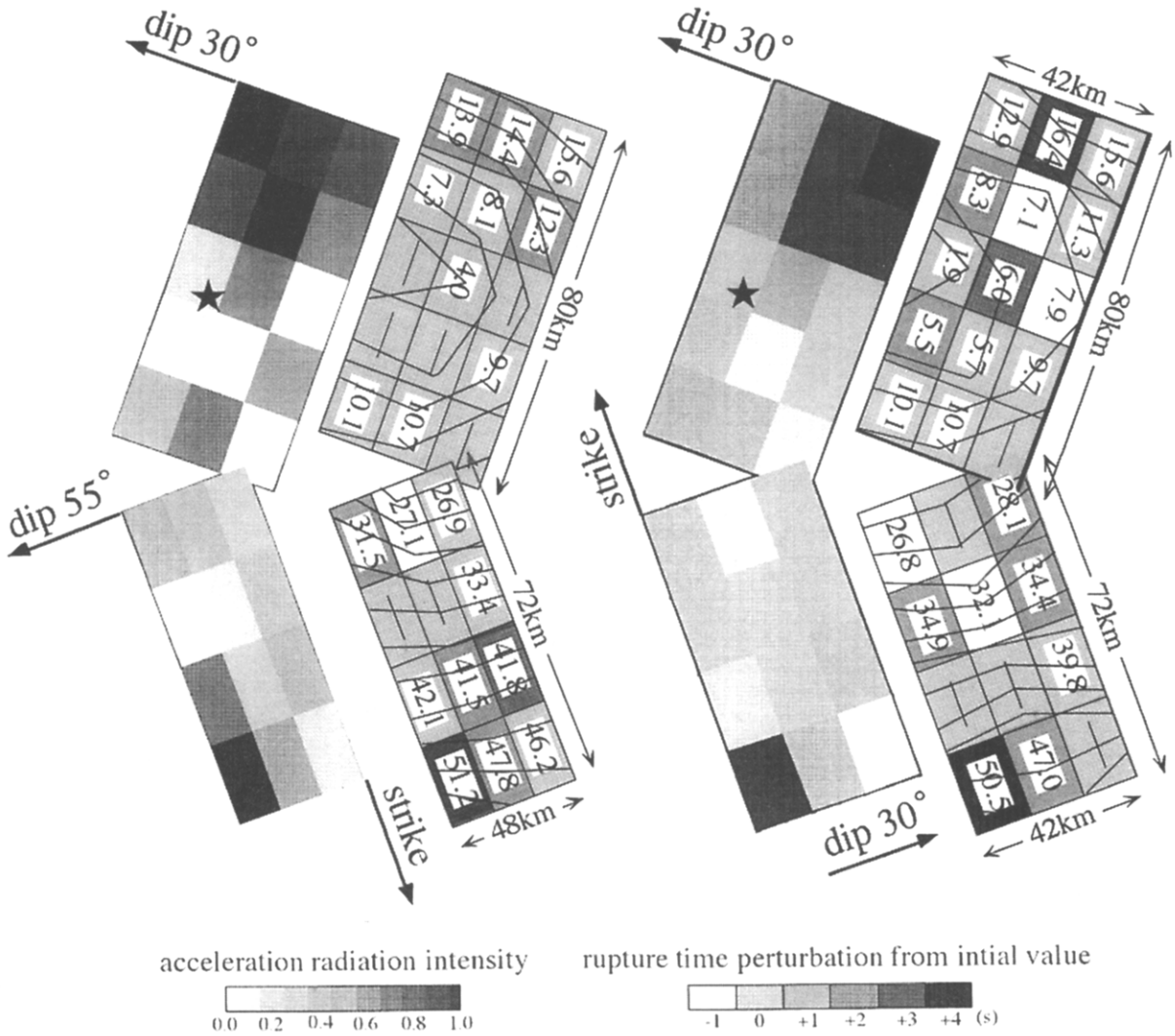

Figure 11. The final solutions for the westward-dipping southern fault (left) and for the eastward-dipping one (right). For each solution, the left and right panels show the acceleration radiation intensities and rupture times (in seconds), respectively. Rupture time values are not shown at the meshes with small radiation acceleration intensities because the contributions of those meshes are small and the rupture times have low reliability.

At the area where the fault changes the strike direction from SSW to SSE, radiation of high-frequency waves is small, though the change of strike direction is expected to behave as a barrier for the rupture. In this area, as mentioned above, we had to put a delay of rupture of 10 sec in the initial model. There is a possibility that the rupture propagated very slowly in this area rather than paused for 10 sec, resulting in small radiation of high-frequency waves.

Kakehi and Irikura (1996) found a complementary distribution of high- and low-frequency wave radiation on the fault plane of the 1993 Kushiro-Oki, Japan, earthquake (M_W = 7.3). The high-frequency radiation was large near the periphery, while the low-frequency radiation was large at the center. This is explained by a simple crack model. Figure 12 shows the comparison of our result with the moment release distribution by Japan Meterological Agency (1995). They also used a model composed of two fault planes. The strike and dip angles of their northern and southern fault planes are (195°, 35°) and (165°, 35°), respectively. The lengths and widths of the two planes are both (75, 39 km). Their result is from the waveform inversion of strong ground displacements with predominant period of about 20 sec, so that it can be interpreted as the distribution of low-frequency wave radiation. There is no clear relation between the distributions of the high- and low-frequency radiation, different from the case of the 1993 Kushiro-Oki earthquake. We interpret this as due to the strong complexity of the rupture.

We perform a resolution and stability test of the inversion as follows. First, we calculate the synthetic envelopes using the final solution obtained above (we call this final

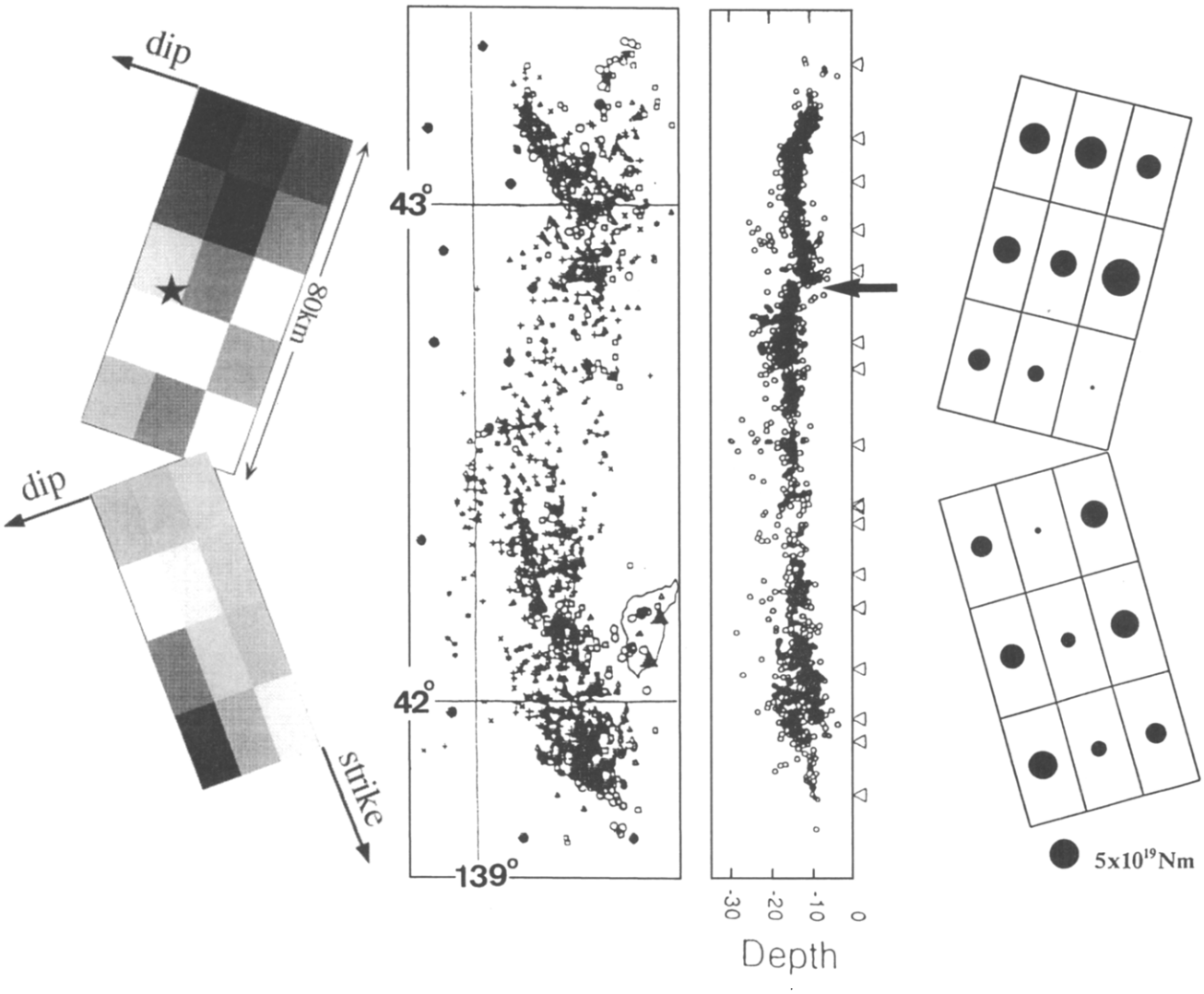

Figure 12. Comparison of the acceleration radiation intensity distribution for the westward-dipping southern fault (left) and the aftershock distribution by Hino *et al.* (1994) (middle). The clear discontinuity in depth distribution is indicated with an arrow. The distribution of the seismic moment release (Japan Meterological Agency, 1995) is also shown for comparison (right).

solution "true solution" hereafter). Then we add 10% random noise to these envelopes. By regarding these noise-added envelopes as the observed data for the test, we perform an inversion to recover the true solution. We use the fault model with the southern fault dipping westward. The initial model for the test inversion is the same as was used for the actual earthquake records. We define the percentage of the noise as the percentage of the area between the noiseless and noise-added envelopes (see the upper panel of Fig. 13) to the area of the noiseless envelopes. The middle panel of Figure 13 shows the noiseless (solid lines) and noise-added envelopes (thin lines). The synthetic envelopes for the solution obtained from the inversion of the noise-added envelopes are shown with thin lines in the lower panel of Figure 13, where the noise-added envelopes are shown with solid lines.

We perform six inversions using different random noises. Figure 14 shows the mean values and the standard deviations of the model parameters obtained in the six inversions. The values in the parentheses are the ones used in the noiseless envelopes, that is, true solution. The resolution and stability is judged by whether these values are recovered well and stably. The meshes whose model parameters satisfy both of the following criteria are drawn with solid lines: (1) the true solution in the parenthesis lies within "mean value +/− standard deviation," and (2) the standard deviations of the acceleration radiation intensity and rupture time perturbation is less than 0.1 and 0.3 sec, respectively.

The model parameters of the northern half part of the southern fault are not recovered well, but they are inverted stably, and the acceleration radiation intensities are estimated to be small, which is consistent with the tendency of

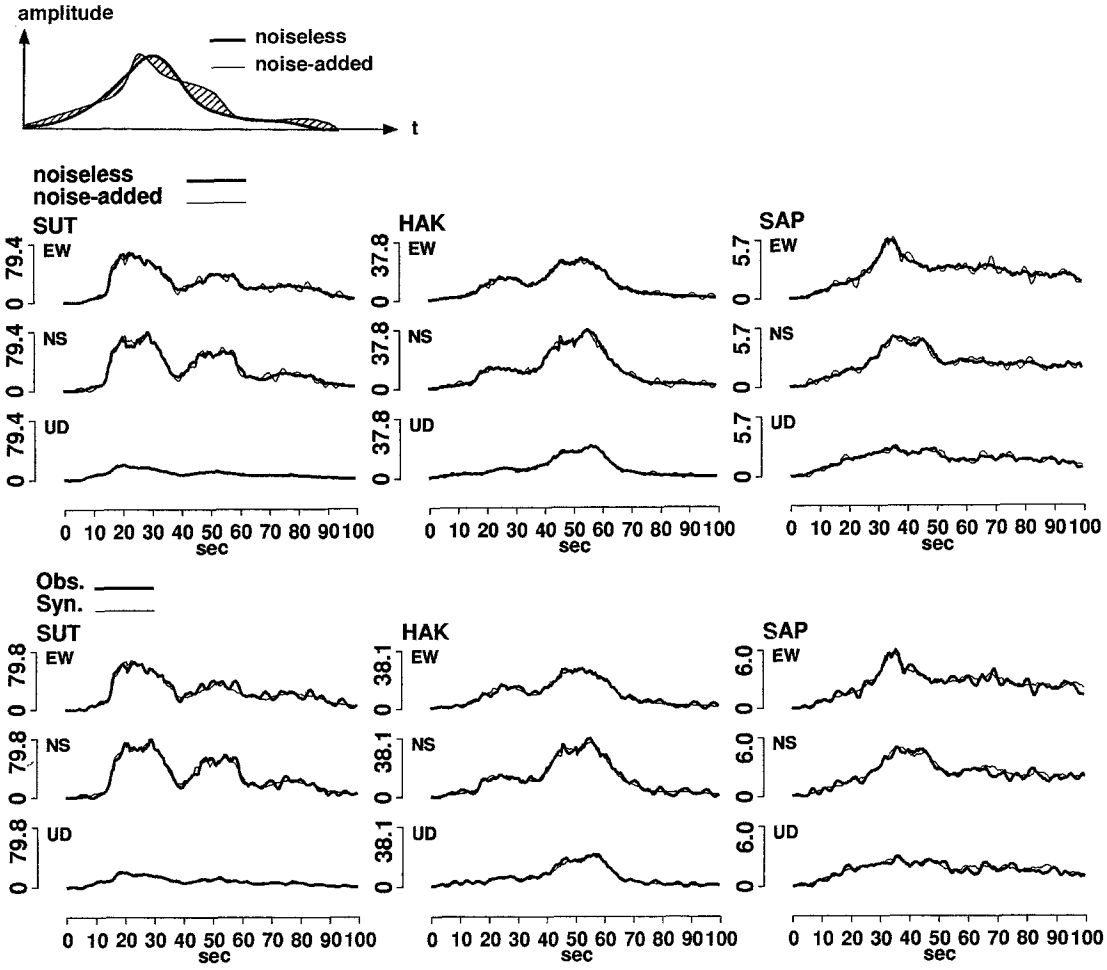

Figure 13. The percentage of the noise added for the resolution and stability test of the inversion is defined as that of the area between the noiseless and noise-added envelopes to the area of the noiseless envelopes (upper). The noiseless (solid lines) and noise-added envelopes (thin lines). The percentage of the noise is 10% (middle). The noise-added envelopes (solid lines) and the synthetic envelopes for the solution obtained from the inversion of the noise-added envelopes (thin lines) (lower).

the true solution. Therefore, it is reliable that the high-frequency wave radiation is not large in this area.

Madariaga (1977) showed theoretically that high-frequency waves are radiated where the rupture velocity changes abruptly. Stopping of rupture is an extreme case. In this study, however, rupture velocity change is not seen in the high-frequency radiation area coincident with the aftershock depth discontinuity. A possible reason is that the mesh size for the inversion is not small enough to detect such rupture velocity change. The relatively large mesh size results from the small number of available stations.

We cannot yet discuss either general characteristics or regional differences about high-frequency wave radiation because only two earthquakes have been analyzed using this method. Such a discussion requires an increase in the number of earthquakes analyzed. Interesting questions include, for example, whether there is a difference between interplate and intraplate earthquakes and whether there is a dependence on magnitude.

By applying our method to high frequencies and the waveform inversion method to low frequencies, we can make a superbroadband (0.01 to 10 Hz, for example) analysis of an earthquake. This will enable us to reproduce the complete rupture history, which will contribute to the understanding of earthquake rupture dynamics.

Acknowledgments

Fujio Kusano of Japan Meteorological Agency and Yoshikazu Kitagawa and Toshihide Kazima of Building Research Institute kindly provided us with the acceleration records. Discussions with Tomotaka Iwata were helpful throughout this study. The manuscript was greatly improved by the valuable comments of the two reviewers. Dr. Alan Linde kindly checked and corrected the English. We are grateful to all of them. This research was supported by the JSPS Fellowships for the Japanese Junior Scientists.

acceleration radiation intensity

NE								SE
0.83±0.10 (0.69)	0.50±0.18 (0.45)	0.03±0.02 (0.00)	0.39±0.02 (0.39)	0.02±0.02 (0.00)	0.31±0.04 (0.24)	0.35±0.12 (0.32)	0.24±0.07 (0.39)	0.50±0.05 (0.37)
0.80±0.06 (0.82)	0.92±0.08 (1.00)	0.50±0.02 (0.50)	0.05±0.06 (0.00)	0.58±0.02 (0.61)	0.25±0.18 (0.37)	0.21±0.08 (0.10)	0.17±0.10 (0.25)	0.56±0.06 (0.52)
0.69±0.13 (1.00)	0.60±0.20 (0.69)	0.20±0.07 (0.10)	0.05±0.04 (0.00)	0.34±0.05 (0.30)	0.33±0.06 (0.48)	0.17±0.06 (0.00)	0.63±0.12 (0.69)	1.00±0.01 (1.00)
NW								SW

rupture time perturbation (s)

NE								SE
0.0±0.3 (0.0)	1.7±0.8 (1.0)	– (–)	0.0±0.1 (0.0)	– (–)	0.0±0.2 (0.0)	0.0±0.3 (0.0)	0.3±0.8 (2.0)	0.2±0.4 (0.0)
1.1±0.3 (1.0)	0.0±0.2 (0.0)	0.0±0.0 (0.0)	– (–)	0.0±0.0 (0.0)	0.0±0.3 (-1.0)	– (–)	0.2±0.7 (1.0)	1.0±0.2 (1.0)
0.4±0.5 (1.0)	0.9±0.9 (0.0)	– (–)	– (–)	0.0±0.1 (0.0)	0.7±0.5 (1.0)	– (–)	0.0±0.3 (0.0)	3.0±0.3 (3.0)
NW								SW

Figure 14. The mean values and standard deviations of the model parameters obtained from the inversions of the six different cases of the envelopes with 10% random noise.

References

Brune, J. N. (1970). Tectonic stress and the spectra of seismic shear waves from earthquakes, *J. Geophys. Res.* **75,** 4997–5009.

Brune, J. N. (1971). Correction, *J. Geophys. Res.* **76,** 5002.

Fukuyama, E. (1994). Source processes of the 1993 Hokkaido-Nansei-Oki earthquake and its largest aftershock, *Kaiyo Monthly, Special Edition for the Hokkaido-Nansei-Oki Earthquake and Tsunamis,* 29–34 (in Japanese).

Fukuyama, E. and K. Irikura (1986). Rupture process of the 1983 Japan Sea (Akita-Oki) earthquake using a waveform inversion method, *Bull. Seism. Soc. Am.* **76,** 1623–1640.

Hartzell, S. H. and T. H. Heaton (1983). Inversion of strong ground motion and teleseismic waveform data for the fault rupture history of the 1979 Imperial Valley, California, earthquake, *Bull. Seism. Soc. Am.* **73,** 1553–1583.

Hashimoto, M., S. Ozawa, A. Yoshimura, T. Sagiya, T. Tada, and H. Tsuji (1994). Crustal movements associated with the 1993 Southwestern off Hokkaido earthquake and its fault model, *Kaiyo Monthly, Special Edition for the Hokkaido-Nansei-Oki Earthquake and Tsunamis,* 55–61 (in Japanese).

Hino, R., T. Kanazawa, K. Suyehiro, T. Sato, and H. Shimamura (1994). Aftershock distribution of the 1993 southwest off Hokkaido earthquake by ocean bottom seismographic array observation, *Kaiyo Monthly, Special Edition for the Hokkaido-Nansei-Oki Earthquake and Tsunamis,* 35–42 (in Japanese).

Hoshiba, M. (1993). Separation of scattering attenuation and intrinsic absorption in Japan using the multiple lapse time window analysis of full seismogram envelope, *J. Geophys. Res.* **98,** 15809–15824.

Hydrographic Survey Team of Hokkaido-Nansei-Oki Earthquake (1994). Preliminary results of the survey on the source region of the Hokkaido-Nansei-Oki earthquake, *Report of Hydrographic Res.* **30,** 395–412 (in Japanese).

Imamura, F., T. Takahashi, and T. Takahashi (1994). Is the fault plane dipping toward the east or west?—interpretation from tsunami data, *Kaiyo Monthly, Special Edition for the Hokkaido-Nansei-Oki Earthquake and Tsunamis,* 179–184 (in Japanese).

Irikura, K. (1986). Prediction of strong acceleration motion using empirical Green's function, *Proc. 7th Japan Earthquake Eng.* **8,** 37–42.

Iwata, T., K. Kamae, and K. Irikura (1994). Source process of the largest aftershock (1993/8/8 M_{JMA} 6.3) of the 1993 Hokkaido-Nansei-Oki earthquake estimated from the near field strong ground motions, *Kaiyo Monthly, Special Edition for the Hokkaido-Nansei-Oki Earthquake and Tsunamis,* 80–87 (in Japanese).

Japan Meteorological Agency (1995). Report on the Hokkaido-Nansei-Oki earthquake, 1993. *Technical Report of the Japan Meteorological Agency* **117** (in Japanese).

Kakehi, Y. and K. Irikura (1996). Estimation of high-frequency wave radiation areas on the fault plane by the envelope inversion of acceleration seismograms, *Geophys. J. Int.* **125,** 892–900.

Kuge, K., M. Kikuchi, and J. Zhang (1994). Complex source process of the July 12, 1993, Hokkaido Nansei-oki earthquake estimated from teleseismic body waves and surface waves, *Kaiyo Monthly, Special Edition for the Hokkaido-Nansei-Oki Earthquake and Tsunamis,* 21–28 (in Japanese).

Kikuchi, M. and Y. Fukao (1985). Iterative deconvolution of complex body waves from great earthquakes—the Tokachi-Oki earthquake of 1968, *Phys. Earth Planet. Interiors* **37,** 235–248.

Kikuchi, M. and H. Kanamori (1991). Inversion of complex body waves—III, *Bull. Seism. Soc. Am.* **81,** 2335–2350.

Lawson, C. L. and R. J. Hanson (1974). *Solving Least Square Problems,* Prentice-Hall, Englewood Cliffs, New Jersey.

Madariaga, R. (1977). High frequency radiation from crack (stress drop) models of earthquake faulting, *Geophys. J. R. Astr. Soc.* **51,** 625–651.

Mendoza, C. and S. H. Hartzell (1989). Slip distribution of the 19 September 1985 Michoacan, Mexico, earthquake: near-source and teleseismic constraints, *Bull. Seism. Soc. Am.* **79,** 655–669.

Nakanishi, I., S. Kodaira, R. Kobayashi, M. Kikuchi, and M. Kasahara (1993). The 1993 Japan Sea Earthquake: quake and tsunamis devastate small town, *EOS* **74,** 377–379.

Takeo, M., S. Ide, and Y. Yoshida (1993). The 1993 Kushiro-Oki, Japan, earthquake: a high stress-drop event in a subducting slab, *Geophys. Res. Lett.* **20,** 2607–2610.

Umino, N. and A. Hasegawa (1994). Aftershock distribution of 1993 south-

west off Hokkaido earthquake estimated from near field sP phase, *Kaiyo Monthly, Special Edition for the Hokkaido-Nansei-Oki Earthquake and Tsunamis,* 49–54 (in Japanese).

Department of Earth and Planetary Sciences
Faculty of Science
Kobe University
Rokkodaicho 1-1, Nada-ku
Kobe 657, Japan
Tel: 81-78-803-0564; fax: 81-78-803-0490
E-mail: kakehi@sc122.earth.s.kobe-u.ac.jp
(Y.K.)

Disaster Prevention Research Institute
Kyoto University
Gokasho, Uji, Kyoto 611, Japan
Tel: 81-774-38-4060; fax: 81-774-33-5866
E-mail: irikura@egmdpri01.dpri.kyoto-u.ac.jp
(K.I.)

Manuscript received 11 November 1994.